ELSEVIER

Chemical Physics 239 (1998) 493–509

Chemical Physics

Photoelectron–photofragment coincidence studies of the dissociative photodetachment of O_4^-

K.A. Hanold [1], R.E. Continetti [*]

Department of Chemistry and Biochemistry, University of California, San Diego, 9500 Gilman Drive, La Jolla, CA 92093-0314, USA

Received 21 July 1998

Abstract

The dissociative photodetachment dynamics of O_4^- ($O_4^- + h\nu \rightarrow O_2 + O_2 + e^-$) have been studied at 532, 355, and 266 nm by triple-coincidence measurements of the energy and angular distributions of the photoelectron and photofragments. The data reveal vibrationally resolved product translational energy distributions and a strong angular correlation between the photoelectron and the photofragments for this direct process. The translational energy distributions show that photodetachment of O_4^- over this photon energy range occurs to several low-lying repulsive states of O_4, producing O_2 in the ground and low-lying electronically excited states ($O_2(X\,^3\Sigma_g^-)$, $O_2(a\,^1\Delta_g)$, and $O_2(b\,^1\Sigma_g^+)$). The partitioning of energy into vibration and rotation of the O_2 products is analyzed in terms of a Franck–Condon model, indicating that the excess electron in O_4^- is delocalized over two identical O_2 moieties in a symmetric O_4^- species. A qualitative analysis of the product angular distributions in terms of the electronic structure of O_4^- is consistent with recent ab initio calculations.

1. Introduction

Dissociation occurs upon photodetachment when a stable anion has Franck–Condon overlap with repulsive regions of the corresponding neutral potential energy surface. For molecular dimer anions [1,2], the corresponding ground-state neutral species are often only bound by a weak van der Waals interaction, so it is expected that this will often occur. In these cases, the neutral will survive for less than a vibrational period and the photoelectron spectrum will be expected to have no discernible structure, providing little insight into the structure of the anion or neutral. To fully characterize such dissociative photodetachment (DPD) processes, a more complete measurement must be made. By combining the techniques of photofragment translational spectroscopy [3] and photoelectron spectroscopy [4], the kinetic energies and recoil angles of the photoelectron and photofragments can be measured in coincidence, providing a complete kinematic characterization of DPD. This paper provides an account of our studies of the dynamics of DPD in O_4^- at 532, 355, and 266 nm, extending a previous brief account of the dynamics of DPD at 532 nm [5]. These results provide important structural insights into O_4^- and the dynamics of dissociation on the O_2–O_2 repulsive surface accessed in photodetachment. The experiments reveal both vibrationally resolved translational energy distributions and evidence of an anisotropic molecular-

* Corresponding author. Fax: +1-619-534-7042.

[1] Present address: Syagen Technology, 1411 Warner Ave., Suite B, Tustin, CA 92780, USA.

0301-0104/98/$ - see front matter
PII: S0301-0104(98)00337-1

frame photoelectron angular distribution in the photodetachment of O_4^- at these wavelengths.

There have been several previous experimental studies of the photochemistry of O_4^-. A thorough review of earlier work on this system is given by Sherwood et al. [6] in a paper concerning the ionic photodissociation of O_4^-: $O_4^- + h\nu \rightarrow O_2 + O_2^-$. Ionic photodissociation is observed to compete with DPD at all wavelengths studied so far, and thus plays an important role in the photodestruction dynamics of O_4^-. At all wavelengths photodissociation is observed to occur via a strong parallel transition, i.e., the products are strongly peaked along the electric vector of the laser. Contributions from the work of Sherwood et al. relevant to the present study include the confirmation of the O_2–O_2^- bond energy $D_0 \approx 0.46$ eV, in accord with mass-spectrometric measurements by Hiraoka [7], and evidence that O_4^- is a doublet radical anion from the observation that the lowest observed photodissociation channel at 532 nm: $O_4^- + h\nu \rightarrow O_2(a\,^1\Delta_g) + O_2^-(X\,^2\Pi_g)$ is spin-forbidden from a quartet ground state.

Other previous studies of O_4^- most relevant to the current DPD experiments include photoelectron spectroscopy and photodestruction measurements by Johnson and co-workers [8–10]. In those experiments, photoelectron spectra were recorded at 532 and 355 nm. The spectra revealed no resolved vibrational structure and showed evidence for a photodissociation channel in the observed photodetachment of nascent O_2^- by a second photon. In our laboratory, low-resolution photoelectron–photofragment coincidence experiments at 523 and 349 nm [11,12] showed that DPD of O_4^- produces O_2 photofragments with wavelength-dependent angular distributions. At 349 nm, DPD yielded both ground-state $O_2(X\,^3\Sigma_g^-) + O_2(X\,^3\Sigma_g^-) + e^-$ and excited-state $O_2(a\,^1\Delta_g) + O_2(X\,^3\Sigma_g^-) + e^-$ products. A third channel that yielded ground-state $O_2(X\,^3\Sigma_g^-) + O_2(X\,^3\Sigma_g^-) + e^-$ products with a higher electron kinetic energy and lower translational energy release was also found at 349 nm. This process, unobserved at 523 nm, originates from a non-Franck–Condon photodetachment process that may derive from an electron–molecule scattering resonance embedded in the $O_2 + O_2 + e^-$ continuum. This is an exception, however, to the direct DPD processes that are the focus of this paper. None of these previous studies, with the exception of the work at 532 nm briefly reported in Ref. [5], had resolution sufficient to reveal O_2 product vibrational distributions or measure photoelectron–photofragment angular correlations.

Previous theoretical studies of O_4^- were limited to semi-empirical or small-basis-set ab initio calculations due to the complexity of the electronic structure of this anion [13–15]. Recently, however, an extensive set of high-level ab initio calculations have been completed by Taylor and co-workers [16]. Using the complete-active-space + second-order perturbation theory method of Bjorn and Roos [17], they obtained predictions for the structure, electron affinity, bond dissociation energy and vibrational frequencies of O_4^-. These calculations predict that the ground state of O_4^- is a doublet and that the molecule is a symmetric species of D_{2h} symmetry, as suggested by the dynamics of DPD at 532 nm [5] and recent density functional theory (DFT) calculations by Chertihin and Andrews [18]. The calculations predict a stability with respect to $O_2 + O_2^-$ of ~ 0.5 eV, in reasonable accord with the experimental quantities [6].

In the following section, the experimental technique of photoelectron–photofragment coincidence spectroscopy is briefly reviewed. This is followed by a presentation of the correlation spectra of the center-of-mass photoelectron kinetic energy (eKE) and center-of-mass photofragment translational energy release (E_T) at 532 nm (2.33 eV), 355 nm (3.49 eV), and 266 nm (4.66 eV). The product internal energy spectra, derived from a measurement of the total kinetic energy release, $E_{TOT} = E_T + eKE$, are presented and analyzed for structural insights into O_4^-. Photoelectron–photofragment angular correlations at all three wavelengths are also presented. In the discussion, an interpretation of the observed dynamics is discussed, providing a schematic picture of ground state of O_4^- and the repulsive states of O_4.

2. Experimental

In these experiments, the DPD of O_4^- is studied in a coincidence measurement of the three photoproducts (electron + two neutral fragments). The experimental method has been previously described [19,20] and will only be briefly reviewed here. A fast

beam of mass-selected O_4^- is intersected with a pulsed laser and the kinematic properties of the photoelectron and neutral fragments are measured in coincidence. A schematic of the apparatus is shown in Fig. 1. The apparatus consists of a mass-selected anion source, a photoelectron spectrometer and a photofragment translational spectrometer capable of detecting neutrals or anions. High detection efficiencies and use of time- and position-sensitive particle detectors for both the photoelectron and molecular fragments allows the correlated measurement of kinetic energy and angular distributions of *all* of the products.

O_4^- is generated by crossing a pulsed supersonic expansion of neat O_2 operating at a repetition rate of 0.6–1 kHz with a 1 keV electron beam. Anions are formed in this source through secondary electron attachment and three-body stabilization [21]. The nascent anions cool in the expansion and pass through a skimmer into a differentially pumped chamber where they are accelerated to a beam energy of 2.5–4 keV. After acceleration, the ion beam is re-referenced to ground potential using a potential switch. Anions are separated according to mass by time-of-flight. Fast neutral particles are removed by guiding the ion beam over a beam block situated on the beam axis. Electrostatic deflectors are employed to direct the ion beam through a 1 mm entrance aperture into the ultra-high-vacuum laser interaction and particle detection region.

Anions at $m/e = 64$ are intersected at a right angle by a laser pulse from the frequency doubled (532 nm), tripled (355 nm), or quadrupled (266 nm) output of a linearly polarized Nd:YAG laser [22]. At a repetition rate of 0.6–1 kHz, the laser yields 200 μJ at 532 nm and 40–60 μJ at either of the ultraviolet wavelengths. The laser pulse is ~100 ps FWHM and is focused to a spot of ~0.5 mm diameter at the point of ion–laser interaction. Absorption of a photon by O_4^- leads to either photodissociation into a neutral and an anionic fragment or DPD into two neutral photofragments and a photoelectron.

Photoelectrons traverse a nominal field-free flight-path of 75 mm and impinge on a 60 mm diameter detector centered perpendicular to the ion beam and laser propagation directions. The laboratory kinetic energy of the electron is measured by time-of-flight and the recoil angle by detected position. Measurement of the electron recoil angle is essential to allow correction for both the Doppler broadening due to the fast ion beam and the actual flight path in the large-solid-angle detector. With these corrections, the electron kinetic energy in the center-of-mass frame (eKE) is determined. The photoelectron spectrometer has an effective angular acceptance of ~4% of 4π sr. The resolution in eKE is ~4% $\Delta E/E$.

Neutral and ionic photofragments can be measured with the photofragment translational spectrometer. Fragments recoil out of the beam over a 96 cm flight path and impinge on a two-particle time- and position-sensitive detector. The ion beam and any charged photofragments are electrostatically deflected off the beam axis in the measurements reported here, so only neutral photofragments are detected. Fragments must clear a 7-mm-wide beam-stop to impinge on the 40-mm-diameter detector microchannel plates. In the work reported at 532 nm,

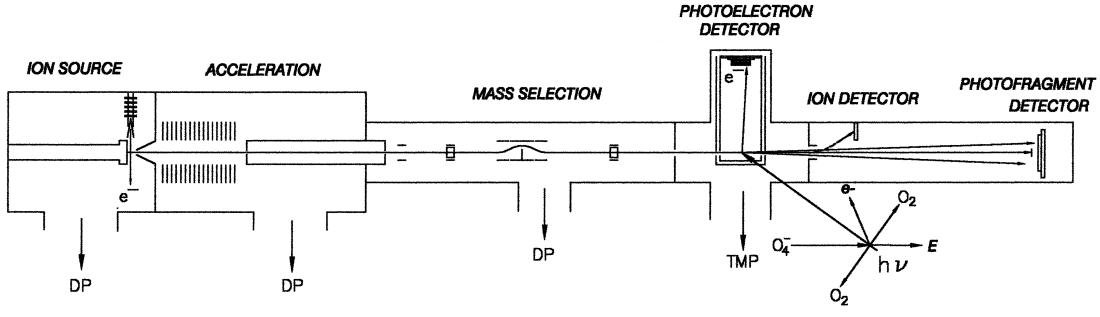

Fig. 1. Schematic of the apparatus, showing the pulsed ion source, acceleration and mass-selection and photodetachment/detection regions. See text for detailed description.

this beam-stop was oriented both horizontally and vertically in successive experiments, permitting a nearly complete measurement of the product angular distributions. At the other wavelengths the beam-block was horizontal. A double wedge-and-strip anode [23] encodes the time- and position-of-arrival of one photofragment striking each half of the detector. This information yields the photofragment mass ratio, center-of-mass translational energy (E_T) and recoil angle for each event [23,24]. Once the mass of the photofragments is determined, the kinetic energy and recoil angle of the photofragments are calculated. The results are then histogrammed in a raw translational energy and angular distribution, $N(E_T, \theta)$. The translational energy resolution is $\leq$ 10% $\Delta E/E$ at $E_T = 0.55$ eV, with a precision of $\sim \pm 0.02$ eV [6]. The angular acceptance of this detector allows for detection of $\sim 80\%$ of the photofragments in coincidence given the kinematics of O_4^- dissociation into $O_2 + O_2 + e^-$. The translational energy distributions reported here are in coincidence with photoelectrons and are raw $N(E_T, \theta)$. The raw $N(E_T, \theta)$ differ from the true center-of-mass $P(E_T, \theta)$ due to the finite angular acceptance of the photofragment detector. A numerical direct-inversion procedure to transform these distributions to $P(E_T, \theta)$ has been previously described [23]. The $P(E_T, \theta)$ reported by Sherwood et al. [11,12] for O_4^- at 523, 349, and 262 nm are very similar to those found in the present experiments. Since the DPD of O_4^- yields equal mass photofragments, with a large E_T, the differences between $N(E_T, \theta)$ and $P(E_T, \theta)$ are small.

Each event is required to consist of two neutral photofragments *or* two neutral photofragments and a photoelectron. Using the time- and position-of-arrival information it can be determined if the two photofragments originate in a single dissociation event by checking for conservation of momentum given the possible dissociation pathways. Correlation of the photoelectron and the neutral photofragments is determined by the spectrometer efficiency and the count rate. To ensure valid photoelectron–photofragment coincidences, the dissociation rate must be $\ll 1$ event per laser pulse. A statistical calculation indicates that with the pulsed spectrometer operating at 600 Hz, and the observed triple coincidence rate of 0.25 Hz, false photoelectron–photofragment coincidences are expected to contribute $\sim 5\%$ to the data [19].

3. Results — Dissociative photodetachment of O_4^- at 532, 355, and 266 nm

The work reported here focuses on the dynamics of the DPD process $O_4^- + h\nu \rightarrow O_2 + O_2 + e^-$. In earlier work, we have reported on photodissociation processes producing stable $O_2^- + O_2$ [6]. Photodissociation followed by autodetachment of internally excited O_2^- is an additional pathway that can yield two O_2 and a free electron [25]. Clear evidence for this process is observed in the 355 nm DPD spectrum described below.

Only equal-mass photofragment pairs were observed. Analysis of data taken under a variety of beam energies and detector positions showed no evidence for other products such as $O_3 + O$ or stable O_4 after photodetachment using photon energies of 2.33, 3.49, and 4.66 eV. In the following sections, we first present the $N(E_T, \mathrm{eKE})$ correlation spectra, followed by the total translational energy release spectra which are contained in the two-dimensional $N(E_T, \mathrm{eKE})$ spectra. The angular correlations of the photoelectron and photofragments at the different wavelengths are then presented.

3.1. Photoelectron–photofragment kinetic energy correlations: $N(E_T, eKE)$ correlation spectra

3.1.1. 532 nm

The $N(E_T, \mathrm{eKE})$ correlation spectrum at 532 nm is shown in Fig. 2 as a two-dimensional histogram of the correlation between electron kinetic energy (eKE) along the *y*-axis and the photofragment translational energy release (E_T) along the *x*-axis. The one-dimensional spectra shown along each axis are obtained by integrating the correlation spectrum over the complementary variable, and represent the photoelectron kinetic energy and photofragment translational energy release spectra measurable in a conventional non-coincidence experiment. The photoelectron spectrum along the *y*-axis shows a broad peak at eKE = 0.7 eV, with some fine structure at higher eKE. The photofragment translational energy release exhibits a broad peak at $E_T = 0.4$ eV, with a

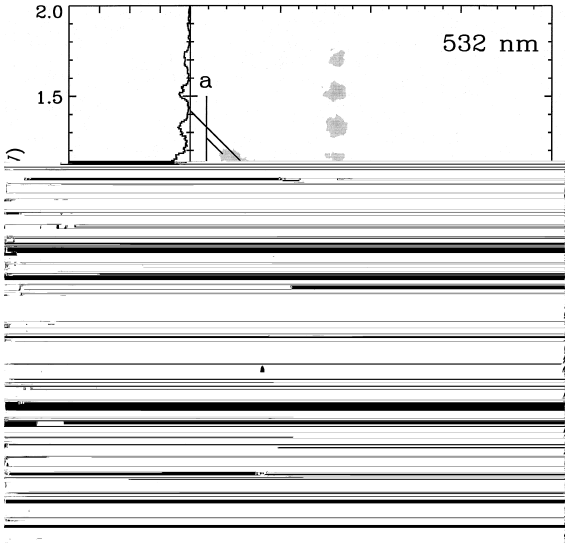

Fig. 2. Photoelectron–photofragment energy correlation spectrum ($N(E_T, \text{eKE})$) for $O_4^- + h\nu \rightarrow O_2 + O_2 + e^-$ at 532 nm. $N(E_T, \text{eKE})$ is represented as a two-dimensional gray-scale histogram. The histogram along the *y*-axis shows the photoelectron spectrum, and the *x*-axis shows the photofragment translational energy distribution. These are obtained by integrating the correlation spectrum over the complementary variable. The features and energetic limits shown are discussed in the text.

small sharper peak at $E_T = 0.8$ eV. The correlation spectrum, however, reveals considerably more information. At 532 nm, the correlation of the broad peaks in the eKE and E_T spectra reveals a series of five diagonal ridges, (marked **a** in the figure), centered at $E_T = 0.4$ eV. There is also a vertical row of spots at $E_T = 0.8$ eV. The eKE spectrum of the spots in the vertical row at $E_T = 0.8$ eV are consistent with the known peaks in the O_2^- photoelectron spectrum [26], as noted in earlier photoelectron spectroscopy measurements by Johnson and co-workers [8–10]. These features arise from a second photon detaching the electron from an $O_2^-(X\,^2\Pi_g)$ photofragment produced in the photodissociation of O_4^- ($O_4^- + h\nu \rightarrow O_2(a\,^1\Delta_g) + O_2^-(X\,^2\Pi_g)$).

The dominant features in the correlation spectrum are the diagonal ridges. Energy conservation dictates that all events that lie within a single diagonal ridge have a well-defined total kinetic energy, ($E_{TOT} = E_T$ + eKE). Within a given ridge, however, there is a range of kinetic energy partitioning between the three products. Using the dissociation energy of O_4^- into $O_2 + O_2^-$ (0.46 eV [7]) and the electron affinity of O_2 (0.45 eV [26]), the maximum translational energy $KE_{MAX} = 1.42$ eV for the DPD process $O_4^- + h\nu \rightarrow O_2(X\,^3\Sigma_g^-, v = 0) + O_2(X\,^3\Sigma_g^-, v = 0) + e^-$ at 532 nm is determined. This is marked as limit (A) in Fig. 2. For the energetics of this DPD pathway as well as others energetically accessible in this work, see Table 1. The ridges are separated by 0.19 eV, which is identified as the vibrational spacing in the O_2 products. The simplest explanation of these features is that they correspond to DPD on vibrationally adiabatic repulsive curves correlating with the different vibrational states of the O_2 products, as discussed further below. Examination of the E_T distribution for each ridge individually shows that the width and shape of the spectrum is independent of product vibrational state.

3.1.2. 355 nm

The 355 nm correlation spectrum is shown in Fig. 3. The channel A observed at 532 nm is observed at this wavelength as well, with an increase in eKE given by the difference of the photon energies at 532 and 355 nm. This shows that Franck–Condon DPD produces $O_2(X\,^3\Sigma_g^-) + O_2(X\,^3\Sigma_g^-) + e^-$ at this wavelength. Evidence for the non-Franck–Condon feature observed at 349 nm producing ground-state O_2 products is seen in the low-energy shoulder in the E_T spectra at 0.2 eV. This feature is much less significant at 355 nm, implying that it is related to a relatively narrow resonance embedded in the DPD continuum. Increasing the photon energy from 2.33 to 3.49 eV also makes new product channels energetically available: the limits B and C correspond to the KE_{MAX} values for production of $O_2(a\,^1\Delta_g) +$

Table 1
Energetics of the low-lying DPD pathways for $O_4^- + h\nu \rightarrow O_2 + O_2 + e^-$

Label	Products	Energy relative to O_4^- (eV)
A	$O_2(X\,^3\Sigma_g^-) + O_2(X\,^3\Sigma_g^-) + e^-$	0.91
B	$O_2(a\,^1\Delta_g) + O_2(X\,^3\sigma_g^-) + e^-$	1.89
C	$O_2(b\,^1\Sigma_g^+) + O_2(X\,^3\Sigma_g^-) + e^-$	2.54
D	$O_2(a\,^1\Delta_g) + O_2(a\,^1\Delta_g) + e^-$	2.87
E	$O_2(b\,^1\Sigma_g^+) + O_2(a\,^1\Delta_g) + e^-$	3.52

Energetics of the excited states of O_2 are taken from Ref. [27].

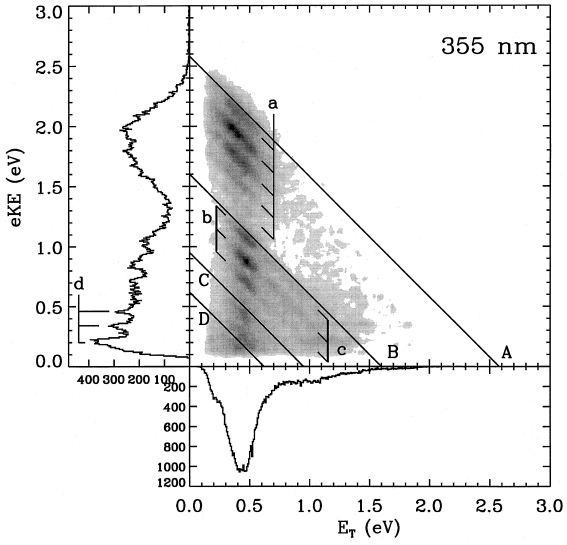

Fig. 3. Photoelectron–photofragment energy correlation spectrum ($N(E_T, \mathrm{eKE})$) for $O_4^- + h\nu \rightarrow O_2 + O_2 + e^-$ at 355 nm. See the text for discussion of the features and energetic limits shown.

$O_2(X\,^3\Sigma) + e^-$ and $O_2(b\,^1\Sigma_g^+) + O_2(X\,^3\Sigma_g^-) + e^-$, respectively. A prominent set of short diagonal ridges is observed beginning below limit B (feature **b**). This is consistent with DPD on vibrationally adiabatic curves corresponding to the production of $O_2(a\,^1\Delta_g) + O_2(X\,^3\Sigma_g^-) + e^-$, with the repulsive energy between the fragments appearing as $E_T = 0.47$ eV. There is also a set of fainter diagonal ridges below maximum B, peaking at $E_T = 0.8$ eV (feature **c**). This implies that there is a second, more repulsive curve producing $O_2(a\,^1\Delta_g) + O_2(X\,^3\Sigma_g^-) + e^-$. Evidence for signal below limit C, corresponding to $O_2(b\,^1\Sigma_g^+, v = 0) + O_2(X\,^3\Sigma_g^-, v = 0) + e^-$, with $E_T \approx 0.4$ eV is also observed. The final observation to be made on the 355 nm spectrum is the appearance of some faint lines parallel to the E_T-axis with $E_T \approx 1$ eV (feature **d**). These features arise from photodissociation of O_4^- producing vibrationally excited O_2^- that undergoes rapid vibrational autodetachment [28] yielding electrons of a well-defined kinetic energy observed in the photoelectron spectra as small sharp peaks superimposed on the broad DPD continuum. The three peaks observed here correspond to autodetachment transitions from $O_2^-(v = 5, 6, 7)$ to $O_2(v = 0)$. Allan and co-workers have recently observed similar phenomena in the dissociative electron attachment to O_3 which yields O + vibrationally excited O_2^- [29].

3.1.3. 266 nm

The 266 nm correlation spectrum is shown in Fig. 4. At 266 nm, pathway A is observed once again, with an increase in eKE corresponding to the increase in the photon energy. The diagonal features in the data for pathway A are not as clearly visible due to the loss of resolution in the TOF measurement for the fast photoelectrons produced at this wavelength. Pathway B is observed to occur only via the more repulsive state observed weakly at 355 nm (feature **c**). The kinetic energy release in this channel peaks at $E_T = 0.8$ eV, as observed at 355 nm. Evidence for signal appearing below limits C (feature **e**) and D (feature **f**) are also observed, indicating that these dissociation pathways are also open. These repulsive curves also appear to yield O_2 products with repulsion on the order of 0.8 eV appearing in translation between the photofragments. It is noted that pathway C has also moved to a higher kinetic energy release ($E_T = 0.8$ eV) compared to 355 nm, implying two distinct repulsive curves yielding products in pathway C as well as B. Laser-correlated background at

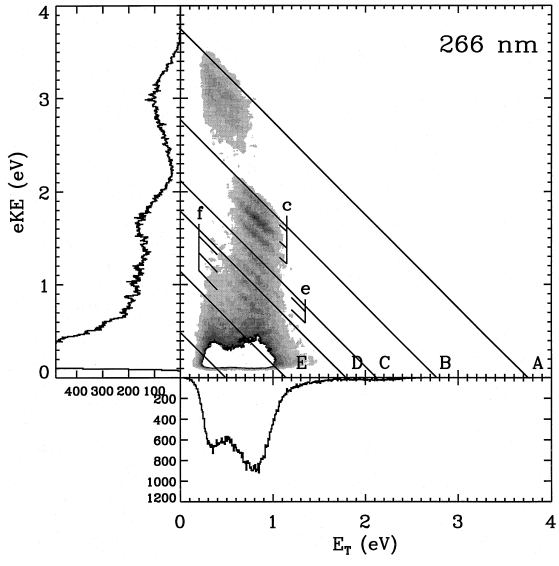

Fig. 4. Photoelectron–photofragment energy correlation spectrum ($N(E_T, \mathrm{eKE})$) for $O_4^- + h\nu \rightarrow O_2 + O_2 + e^-$ at 266 nm. See the text for discussion of the features and energetic limits shown.

eKE < 0.5 eV prevents the observation of autodetachment features at 266 nm. In addition, our previous work has shown that the photodissociation channel at this wavelength is reduced in intensity [6], consistent with the lack of autodetachment signal.

3.2. Total translational energy release and internal energy spectra

Another informative way to view the $N(E_T, \mathrm{eKE})$ correlation spectra is by examination of the total translational energy spectra generated by summing the photoelectron kinetic energy and the translational energy release for each event: $E_{TOT} = \mathrm{eKE} + E_T$. To view the total translational energy release spectra for all the wavelengths on a single graph, it is more convenient to plot them in terms of the product internal energy, $E_{INT} = E_{h\nu} - E_{TOT} - \Delta D_0$, where ΔD_0 is the bond dissociation energy. The E_{INT} spectra at the three wavelengths are shown in Fig. 5. Now the diagonal features in the $N(E_T, \mathrm{eKE})$ spectra appear as a resolved spectrum of the correlated product O_2 vibrational distribution. The energetic limits for the different dissociation pathways from Table 1 are shown on this figure for reference. The 532 nm spectrum shows the best resolution, since the photoelectron resolution degrades significantly with eKE. Examination of the offset of the vibrational peaks from the internal energy origin in this spectrum gives a peak rotational energy summed over the two photofragments of 80 ± 30 meV. The error bars are determined by taking the errors in eKE and E_T in quadrature, along with a 20 meV allowance for the precision of the E_T measurement [6]. The remarkably narrow rotational distribution of the O_2 products implies that O_4^- dissociates from a well-defined structure of high symmetry and thus low exit-channel impact parameter.

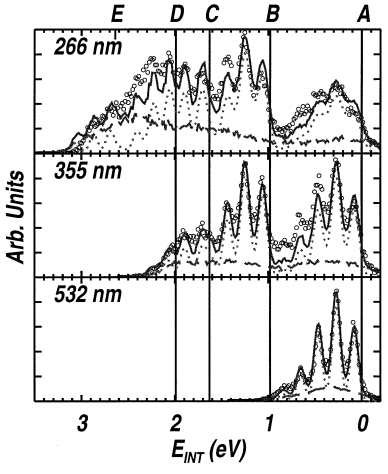

Fig. 5. Vibrationally resolved product internal energy (E_{INT}) spectra for the DPD of O_4^- at 532, 355, and 266 nm as labeled. The product internal energies for the DPD pathways listed in Table 1 are marked as A–E. The open circles correspond to the data, the dotted curves correspond to the local-mode Franck–Condon simulation discussed in the text, and the long-dashed curves correspond to an upper-limit estimate on the non-coincident background in the data. The solid line fit corresponds to the sum of the simulation components.

The fits shown with the spectra consist of two components — one from a local-mode Franck–Condon simulation [5] discussed in further detail below, and a second component, a background feature given by the random correlation of the $N(\mathrm{eKE})$ and $N(E_T)$ spectra. This background feature is scaled to the low (negative) internal-energy tail of the spectra and appears to account for this quite well. With this scaling, the non-coincident background contributes 26%, 28%, and 35% of the total signal at 532, 355, and 266 nm, respectively. This background contribution to the E_{TOT} spectra is significantly larger than the $\sim 5\%$ predicted by the statistical calculation as discussed in the experimental section, and is likely to represent an upper limit. The discrepancy can be attributed to several sources, including overestimation of detection efficiencies and the fact that these large contributions are an overestimate since some of the low-internal-energy tail must originate from internally excited parent anions. Further consideration of the structural implications of the fits will be deferred until a discussion of the Franck–Condon simulation below.

The E_{INT} spectra at 355 and 266 nm are similar, with the exception that the 266 nm spectrum shows a rising signal at large internal energies due to laser-correlated background in the photoelectron spectrum. The similarity between the spectra is remarkable since the correlation spectra show that the pathways (B) and (C) predominantly occur via new, more repulsive O_4 potential energy surfaces at 266 nm. At 266 nm at least two identifiable peaks are observed above the E_{INT} threshold for pathway D, confirming the presence of this dissociation pathway. While

signal is also observed above threshold E, signal in this region dominated by laser-related photoelectron background, so the evidence for occurrence of this dissociation pathway is weak. The observed independence of the product vibrational-state distribution on photon energy suggests that a Franck–Condon transition is depositing neutral O_4 on a repulsive potential energy surface.

3.3. Photoelectron–photofragment angular correlation

The previous section has focused on the insights to gained from examination of the scalar correlation between photoelectron and photofragment kinetic energies. There are other important observables recorded in these experiments, however, including the laboratory angular distributions and the angular correlation of the photoelectron and photofragments. The experiment measures photoelectron and photofragment recoil angles in coincidence, so any correlation between them is expected to be observable in the data. In addition, as our first studies of the DPD of O_4^- at 523 nm showed [11,12], there is a strong alignment of the O_2 products induced by photodetachment, implying dissociation of the molecular framework on a time-scale rapid relative to rotation. Given a rapid dissociation, measurement of the asymptotic product recoil angles provides a measure of the instantaneous alignment of the molecule at the time of photon absorption. Thus, if the photoelectrons are distributed anisotropically in the molecular frame, evidence of this distribution should be directly observable in the data. In the case of O_4^-, such a correlation is observed, as discussed here.

Electric dipole photodetachment or photodissociation of an isotropic ensemble of molecules is known to yield product angular distributions given by the equation [30]

$$I(\theta) = \frac{d\sigma}{d\Omega} = \frac{\sigma}{4\pi}\left[1 + \beta P_2(\cos\theta)\right], \qquad (1)$$

where σ is the total cross-section and $P_2(\cos\theta)$ is a Legendre polynomial. The polar angle between the photofragment-recoil direction and the electric vector of the laser is denoted as θ. The anisotropy parameter β ranges between -1 ($I(\theta) \propto \sin^2\theta$) and $+2$ ($I(\theta) \propto \cos^2\theta$). At 532 nm, both photoelectrons and O_2 photofragments produced in the DPD of O_4^- are preferentially scattered in the plane perpendicular to the $\boldsymbol{E}$ vector ($\beta \approx -0.8$ and -0.5 for photofragments [11,12] and photoelectrons [31], respectively).

In addition to the anisotropic laboratory angular distribution of the photoproducts, a striking angular correlation is observed between the photoelectron and the photofragments at all wavelengths. This angular correlation is most easily visualized by considering the 532 nm data shown in Fig. 6. Frame D shows the relative geometry of the photoelectron-recoil direction and the electric vector of the laser, $\boldsymbol{E}$. In these experiments the ion beam direction was also parallel to the $\boldsymbol{E}$ vector. The sphere shown in frame D indicates the experimentally measured active area of the photofragment detector. Detection of an electron in coincidence requires that the electron recoil into a 25° cone above the plane of the laser and ion beam, breaking the expected cylindrical symmetry of the photofragment angular distribution about $\boldsymbol{E}$ and the ion beam. The E_T-integrated photofragment angular distribution, $N_n(\theta, \phi)$, is extracted by integrating the data over $0 < E_T < 0.6$ eV to give the number of events as a function of θ and ϕ. Here, n denotes the number of particles detected in coincidence; $n = 2$ for $O_2 + O_2$, $n = 3$ for $O_2 + O_2 + e^-$ and ϕ is the azimuthal angle around the $\boldsymbol{E}$ vector. Frame A of Fig. 6 shows a surface-density plot of $N_2(\theta, \phi)$. Given that the O_2 photofragment angular distribution is nearly $\sin^2\theta$, this distribution is a torus. The restricted range of electron recoil angles that can be detected dictates that any angular correlation between the photoelectron and photofragments will break the cylindrical symmetry of $N_2(\theta, \phi)$ about $\boldsymbol{E}$. This occurs, as shown in $N_3(\theta, \phi)$ plotted in frame B of Fig. 6. A pronounced reduction of $O_2 + O_2$ photofragment recoils detected parallel to the direction of photoelectron detection is observed. The existence of this angular correlation shows that photodetachment and dissociation of the nuclear framework of O_4 are both happening on time-scales fast relative to molecular rotation ($\sim$ 1–10 ps), and that the photoelectron preferentially recoils *perpendicular* to the dissociation coordinate in O_4.

The photoelectron–photofragment angular correlation can be further understood by considering the

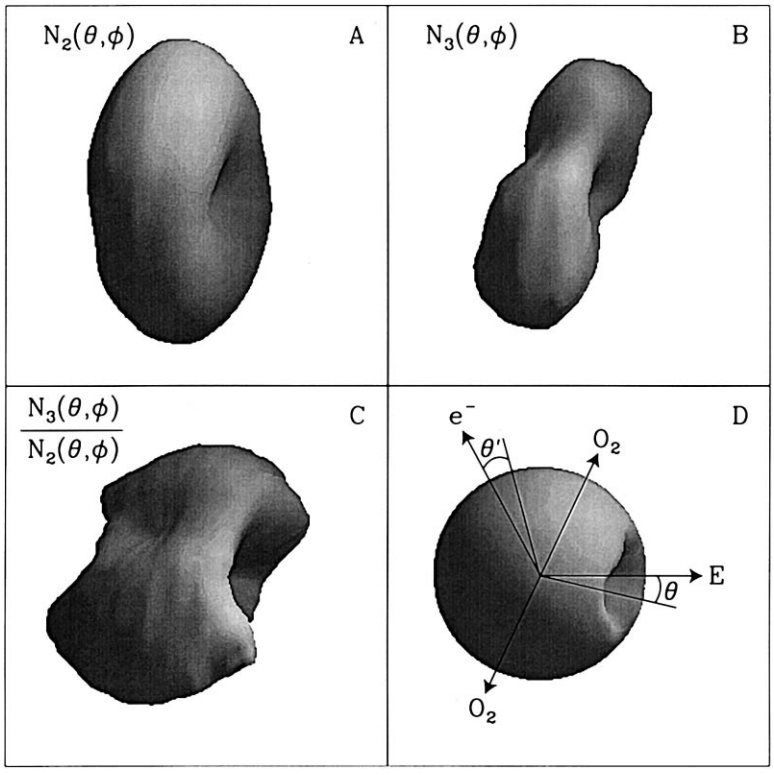

Fig. 6. Surface density plots of the coincident O_2–O_2 photofragment angular distribution illustrating the photoelectron–photofragment angular correlation observed at 532 nm. Frame A shows the O_2-product laboratory angular distribution observed without coincident detection of the photoelectron, $N_2(\theta, \phi)$. This is a $\sin^2\theta$ distribution relative to the laser $\boldsymbol{E}$ vector. Frame B shows the O_2 product angular distribution observed with coincident detection of the photoelectron, $N_3(\theta, \phi)$, showing that the cylindrical symmetry about the $\boldsymbol{E}$ vector is broken. Frame C shows the O_2 product angular distribution in the photoelectron-recoil laboratory frame, obtained from $N_3(\theta, \phi)/N_2(\theta, \phi)$. This is a $\sin^2\theta'$ distribution, now relative to the nominal recoil vector of the photoelectron. Finally, frame D shows the $\boldsymbol{E}$-vector and photoelectron-recoil-vector axes, as well as the effect of the finite detector acceptance on an isotropic product angular distribution.

photofragment angular distribution in the laboratory frame of the photoelectron-recoil direction, as opposed to the direction of the $\boldsymbol{E}$ vector. This distribution is generated by dividing $N_3(\theta, \phi)$ by $N_2(\theta, \phi)$, effectively removing from $N_3(\theta, \phi)$ weighting due to both the photofragment angular distribution in $N_2(\theta, \phi)$ and the finite angular acceptance of the photofragment detector. As frame C of Fig. 6 shows, this photoelectron–electron-recoil-frame product angular distribution is $\propto \sin^2\theta'$, where θ' is now defined as the polar angle of photofragment recoil relative to the nominal photoelectron-recoil direction. The hole in this distribution parallel to $\boldsymbol{E}$ is due to the limited angular acceptance of the photofragment detector, as shown in frame D. A fit to Eq. (1) shows that this distribution is characterized by $\beta_e \approx -0.64$ at 532 nm, as shown in Fig. 7. This value of β_e is expected to be an upper bound on the anisotropy parameter since this treatment of the data assumes that the photoelectron recoils at a single nominal angle in the laboratory frame.

At 355 and 266 nm the photoelectron–photofragment correlation has also been studied. The simplest way to visualize these results is in terms of the photoelectron-recoil-frame product angular distributions discussed in the preceding paragraph. At all wavelengths it is observed that the photofragment angular distribution peaks perpendicular to the nominal recoil direction of the photoelectron. The anisotropy parameters β_e in the photoelectron-recoil-frame, integrated over both eKE and E_T, are shown in Fig. 7 along with the fits to the raw data. The anisotropy

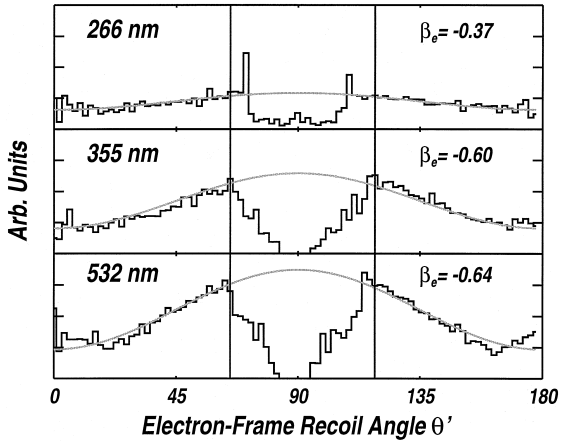

Fig. 7. Photoelectron-recoil-frame O_2 product angular distributions at 532, 355, and 266 nm, generated as in Fig. 6 by dividing $N_3(\theta, \phi)$ by $N_2(\theta, \phi)$. The histogram represents the data, the solid-line curve the fit using Eq. (1), and the vertical bars show the range of angles included in the fit, due to limited detector acceptance. The anisotropy parameters β_e indicate that photofragments preferentially recoil perpendicular to the photoelectron at all wavelengths.

parameters are all less than zero, consistent with photofragment recoil predominantly perpendicular to the recoil direction of the photoelectron.

4. Discussion

The data presented here provide detailed experimental insights into the dynamics of DPD, the repulsive states of O_4, and the structure of O_4^-. No stable states of O_4 were observed from the photodetachment of O_4^-, consistent with the observation of no vibrational structure in the O_4^- photoelectron spectrum. The observation of the diagonal structure in the photoelectron–photofragment $N(E_T, \mathrm{eKE})$ spectra illustrates the value of coincidence measurements for the study of DPD and also provide firm evidence that the DPD of O_4^- is a direct process at these wavelengths, a result that is further confirmed by the strong photoelectron–photofragment angular correlation showing that the dissociation of the molecular framework is much faster than molecular rotation.

Direct DPD alone does not guarantee that diagonal structures will be observed in the correlation spectra. If O_4^- were a diatomic molecule, this would by necessity be true, due to the absence of a broad range of product states in atomic products. Given that two O_2 molecules, with electronic, vibrational, and rotational degrees of freedom are formed, however, it is surprising that the partitioning of energy among the products allows observation of the diagonal structures. This requires formation of products with only a narrow range of product rotational states, indicative of a well-defined structure for O_4^-, with a restricted range of exit-channel impact parameters and thus an angular-momentum-limited product rotational distribution. In the following discussion further insights into the structure of O_4^- are presented first, followed by a discussion of the repulsive neutral O_4 surfaces accessed by photodetachment, and the implications of the photoelectron–photofragment angular correlations on the electronic structure of O_4^-.

4.1. Structural insights — Franck–Condon model for product vibrational energy partitioning

The observation of vibrational structure in the E_{INT} spectra (Fig. 5) allows structural inferences on gas-phase O_4^- to be made. These spectra are a measure of the correlated product vibrational-state distribution. In the 532 nm data, for example, the peak at $E_{INT} = 0.08$ eV corresponds to two $O_2(v = 0)$, the peak at 0.29 eV corresponds to $O_2(v = 0) + O_2(v = 1)$ and the peak at 0.48 eV corresponds to unresolved contributions from both $O_2(v = 1) + O_2(v = 1)$ and $O_2(v = 0) + O_2(v = 2)$ and so forth. Matrix isolation vibrational spectra have been shown to be consistent with two identical O_2 moieties in the O_4^- anion [32]. Taking this as a starting point, we can make the approximation that O_4^- has two important coordinates — the distance between the O_2 moieties and the O–O bond length in each subunit. This local-mode model neglects interaction with the other vibrational degrees of freedom and the detailed form of the normal coordinates for O_4^-. Given this model, a simple simulation was performed by calculating the Franck–Condon overlap of the vibrational wavefunctions of the two 'independent' O_2 moieties in O_4^- with two free $O_2(X\,^3\Sigma_g^-)$ (equilibrium bond length $r_e = 1.207$ Å [27]). The overall Franck–Condon factors for each energetically allowed combina-

tion of vibrational states are calculated as products of the individual diatom Franck–Condon factors. The appropriate weighting for the product state degeneracy must also be accounted for. In the case of $O_2(X\,^3\Sigma_g^-, v=0) + O_2(X\,^3\Sigma_g^-, v=1)$, this degeneracy is two since there are two equivalent ways of forming these products from two indistinguishable O_2 moieties. The diatom Franck–Condon factors were calculated [33] assuming a local-mode O_2 vibrational frequency of 1335 cm^{-1} with an anharmonicity of 8.1 cm^{-1}. The equilibrium bond length, r_e, was then varied to obtain the best fit, with the results plotted as the solid lines in Fig. 5. The agreement between the simulation assuming equal bond lengths of 1.272 Å and the data is excellent at 532 nm. The predicted (uncorrelated) O_2 product vibrational-state distribution for DPD of O_4^- to $O_2(X\,^3\Sigma_g^-) + O_2(X\,^3\Sigma_g^-) + e^-$ is given in Table 2. The sensitivity of the simulation to changes in the bond lengths of the O_2 moieties has been previously shown: for example, a reduction of the bond lengths to 1.26 Å doubles the (0, 0) peak [5]. Simulations of the 355 and 266 nm data are also shown in Fig. 5, illustrating contributions from the higher-lying dissociation asymptotes, $O_2(a\,^1\Delta_g) + O_2(X\,^3\Sigma_g^-) + e^-$, and so forth. While the agreement of the simulation with the data at 355 and 266 nm is not as good as at 532 nm, it is not unreasonable given this simple model. The predicted, uncorrelated O_2 product vibrational distributions for the higher-energy product channels are also shown in Table 2. The overall success of this simple Franck–Condon model in predicting the correlated O_2 product vibrational distributions provides strong evidence that in the gas phase, the excess electron in O_4^- is delocalized over two identical O_2 subunits, with a short O–O bond of 1.272 Å, nearly half way between the ground-state bond lengths of O_2 ($r_e = 1.207$ Å) [27] and O_2^- ($r_e = 1.35$ Å) [27].

Table 2
Relative Franck–Condon factors for photodetachment of O_4^- to two free O_2 molecules, assuming an O–O bond length of 1.272 Å in the identical O_2 moieties constituting O_4^-

Vibrational state	$O_2(X\,^3\Sigma_g^-)$	$O_2(a\,^1\Delta_g)$	$O_2(b\,^1\Sigma_g^+)$
0	1.0	1.0	1.0
1	0.74	0.55	0.33
2	0.23	0.10	0.03
3	0.04	0.01	
4	0.003		

The narrow product rotational distribution inferred from the sharp vibrational features, as discussed above, implies that dissociation of O_4 occurs from a structure with a small exit-channel impact parameter. The $O_2(v=0) + O_2(v=0) + e^-$ feature in the E_{INT} spectrum is found to peak 80 meV above the assigned threshold for this transition. If it is assumed that this rotational energy is shared equally between the two diatom products, a peak value of $J \approx 14$, corresponding to 40 meV in rotation of each O_2, is predicted. This low rotational excitation is not consistent with the trans-planar species of C_{2h} symmetry originally proposed by Conway [13] and later suggested as being consistent with matrix isolation studies [32]. The low rotational excitation is consistent, however, with the recent reinterpretation of the matrix spectra in terms of a planar D_{2h} structure [18], and recent ab initio [16] and density functional [18] calculations.

4.2. The O_2–O_2 distance and characterization of the repulsive states of O_4

As discussed in the last section, the partitioning of internal energy in vibrational and rotational degrees of freedom of the product O_2 molecules provides an insight into the short O–O bonds in O_4^- and the relative configuration of the nuclei. No insight into the O_2–O_2 distance can be gained from that information, however. The eKE and E_T spectra, on the other hand, can provide insights into both the O_2–O_2 coordinate in O_4^- and the repulsive states of the neutral O_4 accessed by photodetachment. The DPD of O_4^- is an example of photoabsorption into two continua — the photoelectron and photofragment dissociation continua. In the absence of energy transfer in the exit channel, the diagonal lines observed in the $N(E_T, eKE)$ correlation spectrum result from projection of the wavefunction describing bound O_4^- onto the repulsive nuclear potential describing $O_2 + O_2 + e^-$ in a bound-to-free Franck–Condon absorption [34]. The measurement of E_T in this case provides information that is complementary to the eKE measurement, since E_T is a direct measure of

the repulsive energy relative to the dissociation asymptote. Since the features are diagonal, the width of the projections unto either the eKE- or E_T-axis are identical. The length of the projection onto these kinetic energy axes is a function of both the equilibrium distance along the bound coordinate in O_4^- and the slope of the repulsive nuclear potential along the reaction coordinate which governs the dissociation of neutral O_4. The steeper the slope of the repulsive potential, the longer the ridge in the $N(E_T, \mathrm{eKE})$ correlation spectrum. Similarly, for a given repulsive state, the larger the range of nuclear geometries in the ground state of O_4^-, the longer the ridge in the $N(E_T, \mathrm{eKE})$ correlation spectrum.

Given a simple model for the O_2–O_2 bond in O_4^-, quantitative information on the repulsive states of O_4 can be extracted. This requires consideration of the bound-free Franck–Condon factors governing DPD. LeRoy and co-workers [35,36] have developed a formalism for calculating bound-free Franck–Condon factors for diatomic molecules, originally to model continuum absorption coefficients. They take the bound-free FCF as the photodissociation cross-section, defined in terms of the radial matrix elements between the bound and continuum states of a diatomic molecule as follows:

$$\sigma_\nu(v, J, E) \propto C\nu G_{\mathrm{el}} \left| \langle \psi_{E,J} | M(R) | \psi_{v,J} \rangle \right|^2 . \qquad (2)$$

In this equation $\psi_{v,J}$ is the bound-state wavefunction for a given vibrational (v) and rotational (J) state and $\psi_{E,J}$ is an appropriately normalized continuum wavefunction for the dissociation of a diatom into two atoms with a kinetic energy E. $M(R)$ is the transition dipole function, which in general is radially dependent. C is a constant, ν is the frequency of the excitation, and G_{el} is the ratio of final-state to initial-state electronic degeneracies. The assumptions made in applying this formalism to the interpretation of DPD are significant. Beyond the approximation of O_4^- as a pseudo-diatomic molecule, discussed in the next paragraph, the continuum wavefunction in the case of DPD should be rigorously treated as a product of the electron and nuclear continuum wavefunctions. Detailed theoretical treatments of the bound-continuum Franck–Condon factors in the case of DPD have recently been reported for the $ClHCl^- \rightarrow Cl + HCl + e^-$ system, as discussed by Takatsuka [37] and Balint-Kurti and Schatz [38]. In the future, generalization and application of these formalisms to the DPD of O_4^-, in which a free electron and two diatomic molecules are produced, will provide a more accurate description of the dynamics of this bound-free process. For present purposes, however, only an approximate measure of the slope of the repulsive neutral surfaces accessed in this experiment is sought, so the LeRoy formalism should suffice.

Continuing with the two-coordinate model introduced in Section 4.1, we approximate O_4^- as a pseudo-diatomic molecule along the coordinate connecting the O_2 centers of mass in O_4^-. To apply the formalism, an approximate bound potential for $[O_2$–$O_2]^-$ can be obtained from the detailed ab initio calculations of Taylor and co-workers [16], assuming that the totally symmetric 371 cm^{-1} vibration most closely approximates the $[O_2$–$O_2]^-$ coordinate. Modeling this vibration as a Morse potential,

$$V(r) = \varepsilon\left(e^{-\beta(r-r_0)} - 1\right)^2 \qquad (3)$$

with classical well-depth $\varepsilon = 3896$ cm^{-1}, $r_e = 2.108$ Å and $\beta = 4.08$ $Å^{-1}$, yields a potential with classical turning points for $v = 0$ at 2.05 and 2.16 Å. The extent of this ground vibrational-state wavefunction determines the region of the excited-state potential energy surface sampled in photodetachment. Using the BCONT program developed by LeRoy [35,36] to model photodetachment from the ground vibrational state of this one-dimensional Morse potential to repulsive excited-state curves, we can fit the kinetic energy distributions given by the projection of the diagonal features in the correlation spectra onto either the eKE- or E_T-axis. The fits were performed for the $(v = 0, v = 0)$ eKE distributions from the correlation spectra, in feature **a** at 532 nm, feature **b** at 355 nm and feature **c** at 266 nm.

The results of these fits are shown as the solid line fits to the eKE data points plotted vertically on the potential energy diagram in Fig. 8, with the best-fit excited-state Morse parameters shown in Table 3. These curves are all repulsive in the region of Franck–Condon overlap with a small well at large distances of 75 cm^{-1}. This is qualitatively consistent with the van der Waals well-depth for the ground state of $(O_2)_2$ reported by Long and Ewing [39] to be

87 cm^{-1}. No attempt was made to account for the radial dependence of the transition moment, and due to the significant approximations inherent in treating the DPD of O_4^- with a diatomic molecule code, these potentials should not be regarded as unique. Nonetheless, these potential energy curves represent one of the first experimental measures of the low-lying repulsive states of O_4. In Fig. 8 the vertical energy spectrum of the repulsive excited states is shown relative to the O_4^- ground state at 0 eV. The dissociation asymptotes A and B are also shown in this figure, showing that the repulsion for feature **a** in the coincidence spectra, correlating to $O_2(X^3\Sigma_g^-) + O_2(X^3\Sigma_g^-) + e^-$, peaks at $E_T \approx 0.4$ eV. The next observed state, correlating to $O_2(a^1\Delta_g) + O_2(X^3\Sigma_g^-) + e^-$, peaks at $E_T \approx 0.47$ eV, while the higher energy state correlating to this asymptote, most clearly observed at 266 nm, peaks at $E_T \approx 0.8$ eV. As noted in the discussion of the $N(E_T, \mathrm{eKE})$ spectra, evidence is also observed for at least two repulsive states correlating to $O_2(b^1\Sigma_g^+, v = 0) + O_2(X^3\Sigma_g^-, v = 0) + e^-$ with similar slopes and mean repulsion as the $O_2(a^1\Delta_g) + O_2(X^3\Sigma_g^-) + e^-$ curves. However, the quality of the data for these higher-energy repulsive states is degraded by laser-related background in the 266 nm spectrum, so a simulation of those data has not been attempted.

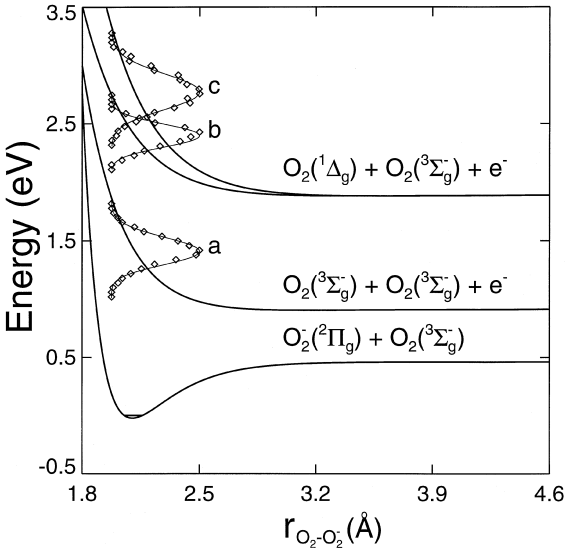

Fig. 8. Schematic of the Morse potentials used to represent the ground state of O_4^- and the low-lying states of O_4 as a pseudo-diatomic molecule in the bound-free Franck–Condon calculation discussed in the text. The photoelectron spectra for the $O_2(v = 0) + O_2(v = 0)$ peak of the features **a** (532 nm), **b** (355 nm) and **c** (266 nm) in the correlation spectra are shown as the diamonds along the vertical scale, with the fits shown as the thin solid curves.

Table 3
Best-fit Morse parameters for the bound-free Franck–Condon simulation of the DPD of O_4^-, treating O_4^- and neutral O_4 as pseudo-diatomic molecules (O_2–O_2) with a reduced mass of 16 amu

Dissociation asymptote	ε (cm^{-1})	r_e (Å)	β ($Å^{-1}$)
$O_2^-(X^2\Pi_g) + O_2(X^3\Sigma_g^-)$	3896	2.10	4.08
$O_2(X^3\Sigma_g^-) + O_2(X^3\Sigma_g^-) + e^-$	75	3.15	2.05
$O_2(a^1\Delta_g) + O_2(X^3\Sigma_g^-) + e^-$	75	3.40	1.66
$O_2(a^1\Delta_g) + O_2(X^3\Sigma_g^-) + e^-$	75	3.59	1.61

Potential energy curves and fits to the data are shown in Fig. 8.

The fact that DPD provides an experimental characterization of the repulsive curves of O_4 should provide an important test of the neutral O_2–O_2 potential energy surface. Preliminary calculations by Taylor and co-workers are consistent with these experimental observations, showing that the repulsion between $O_2(^3\Sigma_g^-)$ and $O_2(^3\Sigma_g^-)$ at the geometry of the O_4^- ground state is ~ 0.4 eV. It will be of interest to compare these experimental results to global O_2–O_2 potential energy surfaces [40,41] when a more complete theoretical treatment of DPD is available and applied to O_4^-.

4.3. The electronic structure of O_4^- and angular distributions in dissociative photodetachment

Recent ab initio calculations by Aquino et al. [16] and DFT calculations by Chertihin and Andrews [18] agree that the ground state of O_4^- has D_{2h} symmetry with a ^2A_u electronic ground state. The ab initio calculations yield a stability of O_4^- with respect to $O_2(^3\Sigma_g^-) + O_2^-(^2\Pi_g)$ of ~ 0.50 eV, in reasonable agreement with the experimental quantities. The DFT calculations, on the other hand, indicate a stability of only 0.2 eV. The dominant configuration of the ^2A_u ground state can be understood by considering overlap of the π_g anti-bonding orbitals of O_2 and O_2^- as shown in Fig. 9. This simple molecular orbital pic-

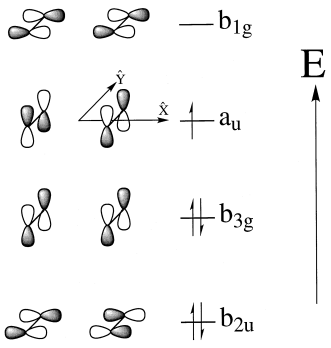

Fig. 9. A schematic diagram of the valence orbitals for O_4^-, formed by interaction of the π_g anti-bonding orbitals of O_2 and O_2^-.

ture is consistent with an analogous discussion of the O_4^+ given by Griffith and Gellene [42]. Using this MO configuration, which is the same as the dominant configuration calculated by Aquino et al. [16], the lowest repulsive curve of O_4 accessed by photodetachment is expected to be a singlet state produced by removal of the lone electron in the a_u highest-occupied molecular orbital (HOMO) of the anion. The other curves, correlating to singlet + triplet O_2 are low-lying triplet states of O_4 resulting from photodetachment of electrons in the b_{3g} and b_{2u} orbitals. This single configuration picture, however, is only approximate due to the highly multiconfigurational nature of the electronic structure of O_4^-.

The implications of the electronic structure of O_4^- for the photoelectron and photofragment angular distributions can now be examined. This requires a consideration of the dipole selection rules for photodetachment of molecular anions. The dipole selection rules for atomic anions are particularly straightforward, $\Delta l = \pm 1$, owing to the fact that the electronic orbital angular momentum, l, is a good quantum number in a central potential [43]. In a polyatomic molecular anion, however, l is no longer well-defined, and a detailed treatment of the photodetachment dynamics entails a high-level electron–molecule scattering calculation. In lieu of this detailed treatment, the formalism of Brauman and co-workers [44] for evaluation of photodetachment cross-sections and continuum dipole selection rules for polyatomic molecules can be applied to O_4^-.

Their work showed that if the photodetached electron and the resulting molecular core can be treated in a one-electron approximation, the allowed continuum states for photodetachment are those for which the direct product of the symmetry of the HOMO, the transition dipole μ_x, μ_y, or μ_z, and the final state is the totally symmetric irreducible representation. The overall symmetry of the final state reached in photodetachment is determined by the direct product of the symmetry of the electron continuum and the neutral core. For the a_u HOMO given by the dominant configuration of O_4^-, dipole-allowed final states in D_{2h} symmetry are $B_{3g}(x)$, $B_{2g}(y)$ and $B_{1g}(z)$, where the x, y and z denote the symmetry axis of the transition dipole. At 532 nm, the transition moment for DPD must lie along either the y- or z-axis, since the photofragments are preferentially scattered in the plane perpendicular to the electric vector of the laser. Thus, given that the symmetry of the molecular core after photodetachment of the a_u electron is ^1A_g, the photoelectron continua must be of either $B_{2g}(y)$ or $B_{1g}(z)$ symmetry. These irreducible representations transform like d_{xz} and d_{xy} orbitals, respectively. This is consistent with the observation at 532 nm that the photoelectron angular distribution peaks perpendicular to the laser electric vector, indicating that a strong preference for d-wave photodetachment is observed, even at a photon energy 1.42 eV above threshold.

The conclusion that d-wave photodetachment will dominate near threshold for a system with the electronic structure of O_4^- can also be directly reached by qualitative consideration of the a_u HOMO for O_4^- shown in Fig. 9. This HOMO has three angular nodes, and is thus analogous to an atomic f orbital, resulting in both d ($l = 2$) and g-wave ($l = 4$) photodetachment. This situation was discussed in a study by Gygax et al. [45] of the photodetachment cross-section for the cyclooctatetraene anion. They showed that the photodetachment cross-section from the f-like HOMO of this anion is consistent near threshold with a d-wave photoelectron continuum. Above threshold, however, the higher angular momentum states of the photoelectron continuum are accessible and will lead to an energy-dependent photoelectron angular distribution. This, and the contributions of new product electronic states, is likely to be the cause of the energy dependence observed in the photoelectron-recoil-frame angular distributions in Fig. 7.

The strong photofragment–photoelectron angular correlation observed indicates a highly anisotropic molecular-frame photoelectron angular distribution (MF-PAD). The mere observation of the photoelectron–photofragment angular correlation shows that dissociation occurs promptly on the time-scale of molecular rotation. Thus, the recoil direction of the O_2–O_2 photofragments provides a record of the alignment of the dissociation coordinate at the time of photon absorption. It is well-known that studying the MF-PAD can provide detailed insights into photoionization processes, since photoelectron angular distributions are governed by both the magnitude and relative phases of the degenerate electron continuum channels [43]. As first discussed by Dill [46], and extended in recent years by Chandra [47], Rudolph and McKoy [48], and Park and Zare [49,50], the MF-PAD contains more detailed information than a laboratory-frame angular distribution due to the removal of the averaging over the orientation of the transition moment relative to the laser $\boldsymbol{E}$ vector. This has been exploited experimentally in studies of dissociative photoionization by Dehmer and Dill [51], Golovin et al. [52], Powis and co-workers [53,54], Kaesdorf et al. [55], and Shigemasa et al. [56,57]. Zare and co-workers have also studied the MF-PAD by vibrational and rotational state-selective photoionization of dipole-aligned NO, providing a detailed partial-wave decomposition of the photoelectron continuum [49,50].

Dill [46] showed that photoelectron angular distribution for a space-fixed molecule, in contrast to Eq. (1) is given by:

$$\frac{\mathrm{d}\sigma(E)}{\mathrm{d}\Omega} = \sum_{l=0}^{2l_{\max}} \sum_{m} A_{lm}(E) Y_{lm}(\vartheta, \varphi) . \qquad (4)$$

In this equation, $l_{\max}$ is the maximum value for the photodetached electron orbital angular momentum and m corresponds to the azimuthal quantum number for the photodetached electron. The spherical harmonics $Y_{lm}(\vartheta, \varphi)$ are referenced to the molecular frame by the polar and azimuthal angles ϑ, φ. Since the sum ranges from $l = 0$ to $2l_{\max}$, odd harmonics can contribute to the MF-PAD, yielding more complicated photoelectron angular distributions. The magnitudes of the coefficients $A_{lm}(E)$ are in general energy dependent and are determined by electric-dipole selection rules and interference between the degenerate photoelectron continuum channels. In addition to determining the relative contributions of the spherical harmonics Y_{lm}, these coefficients contain detailed information on both the photodetachment dynamics and the orbital from which the electron is ejected. The strong angular correlation observed between photoelectron and photofragments in these experiments indicates that the photoelectron continuum is dominated by a restricted set of partial waves. Due to the multiconfigurational character of the ground electronic state of O_4^-, a detailed analysis of the photoelectron continuum will not be attempted here. Nonetheless, the DPD of O_4^- provides the first observation of an anisotropic MF-PAD in photodetachment of a negative ion. With future improvements in electronic structure and electron–molecule scattering calculations, it is hoped that a more complete interpretation of the anisotropic MF-PADs observed in the DPD of O_4^- will be possible in the future.

4.4. Implications for bound excited states of O_4

A final issue on which the results reported in this paper have some bearing is the question of possible bound states of neutral O_4. Several calculations have indicated that a bound excited state of O_4, with potential application as an energetic material, may exist [58,59]. The van der Waals $(O_2)_2$ cluster in the ground electronic state was characterized by Long and Ewing [39], excited electronic states were studied by Goodman and Brus [60,61], and more recent studies of $(O_2)_2$ include VUV photoionization studies by Ukai et al. [62] and Carnovale et al. [63]. The binding energy of the neutral dimer in the ground state is estimated to be 90 cm^{-1}, with an O_2–O_2 distance of 4.8 Å [39]. The large difference in geometries between this neutral dimer and the ground state of O_4^- leads to the formation of no stable dimer on the ground electronic state by photodetachment. Evidence for both repulsive and relatively long-lived excited states (10^{-13}–10^{-7} ws) of O_4 has been found by Helm and Walter using charge exchange of O_4^+ with various electron-donor targets [64]. Charge-exchange neutralization of the cation probes different neutral geometries and can also access much higher energy states of the neutral than the photodetachment

experiments reported here, which are restricted by the electron affinity and photon energy to probing configurations < 3.7 eV above the energy of two separated O_2 molecules. There has also been a recent report by Suits and co-workers [65] concerning photoionization of O_4. These experiments, using mass-resolved multiphoton ionization techniques and photoelectron spectroscopy to study a discharge-excited O_2 molecular beam, have yielded spectra that have been tentatively assigned to metastable excited states of O_4. Their results have been interpreted in terms of the calculations to date that predict potentially bound excited states of O_4 are either of D_{2d} or D_{3h} symmetry [58,59]. The difference in symmetry makes it doubtful that there would be significant Franck–Condon overlap for photodetachment from the D_{2h} O_4^- anion.

5. Conclusions

This paper reports high-resolution photoelectron–photofragment coincidence studies of O_4^- at 532, 355, and 266 nm. This work, combined with our earlier study of the ionic photodissociation dynamics of O_4^- in this wavelength region, provides an extensive experimental characterization of the photodestruction dynamics of O_4^- and insights into the ground state of gas-phase O_4^- and the repulsive states of both O_4^- and O_4. The rich photochemistry observed for O_4^- is a consequence of the number of low-lying ionic and neutral electronic states available to the oxygen dimer. This results in a system that provides significant challenges for quantum chemistry and reaction dynamics theory, and we hope that these experimental results will motivate further theoretical studies of this system to provide a fundamental understanding of the photochemistry of O_4^-.

On a general level, these experiments provide a fine example of the utility of photoelectron–photofragment coincidence measurements in the study of a direct DPD process. Direct DPD is expected to be common in systems with a weakly bound neutral ground state and a strongly bound anionic ground state. The DPD of O_4^- provides the best example observed to date of such direct DPD processes, wherein dissociation occurs much faster than molecular rotation, and more likely on the time-scale of molecular vibration. Without the coincidence measurement, a determination of the partitioning of kinetic energy between the photoelectron and photofragments is not possible in such DPD processes. In the case of O_4^- the partitioning of kinetic energy reveals the correlated O_2 product vibrational distribution. Furthermore, the coincidence measurement of photofragment and photoelectron angular distributions provides a practical means of observing anisotropic molecular-frame photoelectron angular distributions in anions that undergo direct DPD. These measurements have the potential to extend to anionic systems some of the insights gained by studying the dynamics of photoionization in stable neutral molecules in recent years.

Acknowledgements

This work was supported by the Chemistry Division of the National Science Foundation under grant CHE 97-00142. REC is a Camille Dreyfus Teacher-Scholar, and Alfred P. Sloan Research Fellow and a Packard Fellow in Science and Engineering. We acknowledge contributions by Mark Garner towards data collection, and thank Drs. Aquino, Walch and Taylor for access to their unpublished calculations.

References

[1] S.T. Arnold, J.G. Eaton, D. Patel-Misra, H.W. Sarkas, K.H. Bowen, in: J.P. Maier (Ed.), Ion and Cluster Ion Spectroscopy and Structure, Elsevier, New York, 1989, pp. 417–472.
[2] P.B. Comita, J.I. Brauman, J. Am. Chem. Soc. 109 (1987) 7591.
[3] J.M. Farrar, in: T. Baer, C.Y. Ng, I. Powis (Eds.), Cluster Ions, Wiley, New York, 1993, pp. 243–317.
[4] K.M. Ervin, W.C. Lineberger, in: N.G. Adams, L.M. Babcock (Eds.), Advances in Gas Phase Ion Chemistry, vol. 1, JAI Press, Greenwich, CT, 1992.
[5] K.A. Hanold, M.C. Garner, R.E. Continetti, Phys. Rev. Lett. 77 (1996) 3335.
[6] C.R. Sherwood, K.A. Hanold, M.C. Garner, K.M. Strong, R.E. Continetti, J. Chem. Phys. 105 (1996) 10803.
[7] K. Hiraoka, J. Phys. Chem. 89 (1988) 3190.
[8] L.A. Posey, M.J. Deluca, M.A. Johnson, Chem. Phys. Lett. 131 (1986) 170.
[9] M.J. DeLuca, C.C. Han, M.A. Johnson, J. Chem. Phys. 93 (1990) 268.

[10] C.C. Han, M.A. Johnson, Chem. Phys. Lett. 189 (1992) 460.
[11] C.R. Sherwood, M.C. Garner, K.A. Hanold, K.M. Strong, R.E. Continetti, J. Chem. Phys. 102 (1995) 6949.
[12] K.A. Hanold, C.R. Sherwood, R.E. Continetti, J. Chem. Phys. 103 (1995) 9876.
[13] D.C. Conway, J. Chem. Phys. 50 (1969) 3864.
[14] K. Ohta, K. Morokuma, J. Phys. Chem. 91 (1987) 401.
[15] X.Y. Li, A.M. Tian, F.C. He, G.S. Yan, Chem. Phys. Lett. 233 (1995) 227.
[16] A. Aquino, S.P. Walch, P.R. Taylor (to be published).
[17] K. Andersson, B.O. Roos, in: D. Yarkony (Ed.), Modern Electronic Structure Theory, Part 1, World Scientific, Singapore, 1995.
[18] G.V. Chertihin, L. Andrews, J. Chem. Phys. 108 (1998) 6404.
[19] R.E. Continetti, Int. Rev. Phys. Chem. 17 (1998) 227.
[20] K.A. Hanold, C.R. Sherwood, M.C. Garner, R.E. Continetti, Rev. Sci. Instrum. 66 (1995) 5507.
[21] M.A. Johnson, W.C. Lineberger, in: J.M. Farrar, W.H. Saunders (Eds.), Techniques in Chemistry 20 (1988) 591.
[22] X. Xie, J.D. Simon, Opt. Commun. 69 (1989) 303.
[23] R.E. Continetti, D.R. Cyr, D.L. Osborn, D.J. Leahy, D.M. Neumark, J. Chem. Phys. 99 (1993) 2616.
[24] D.P. DeBruijn, J. Los, Rev. Sci. Instrum. 53 (1982) 1020.
[25] R.J. Li, K.A. Hanold, M.C. Garner, A.K. Luong, R.E. Continetti, Faraday Discuss. Chem. Soc. 108 (1997) 115.
[26] M.J. Travers, D.C. Cowles, G.B. Ellison, Chem. Phys. Lett. 164 (1989) 449.
[27] K.P. Huber, G. Herzberg, Molecular Spectra and Molecular Structure IV, Van Nostrand, New York, 1979, p.490.
[28] G.J. Schulz, Rev. Mod. Phys. 45 (1973) 423.
[29] M. Allan, J. Phys. B: At. Mol. Opt. Phys. 28 (1995) 5163.
[30] R.N. Zare, Mol. Photochem. 4 (1972) 1.
[31] C.R. Sherwood, Ph.D. Thesis, University of California, San Diego, CA, 1995.
[32] L. Manceron, A.-M. Le Quere, J.-P. Perchard, J. Phys. Chem. 93 (1989) 2960.
[33] K.M. Ervin, J. Ho, W.C. Lineberger, J. Phys. Chem. 92 (1988) 5405.
[34] J. Tellinghuisen, in: K.P. Lawley (Ed.), Photodissociation and Photoionization, Wiley, New York, 1985, pp. 299–369.
[35] R.J. Le Roy, R.G. Macdonald, G. Burns, J. Chem. Phys. 65 (1976) 1485.
[36] R.J. Le Roy, Comput. Phys. Commun. 52 (1989) 383.
[37] K. Takatsuka, Phys. Rev. A 55 (1997) 347.
[38] G.G. Balint-Kurti, G.C. Schatz, J. Chem. Soc., Faraday Trans. 93 (1997) 755.
[39] C.A. Long, G.E. Ewing, J. Chem. Phys. 58 (1973) 4824.
[40] P.E.S. Wormer, A. van der Avoird, J. Chem. Phys. 81 (1984) 1929.
[41] D. Lauvergnat, D.C. Clary, J. Chem. Phys. 108 (1998) 3566.
[42] K.S. Griffith, G.I. Gellene, J. Chem. Phys. 96 (1992) 4403.
[43] J. Cooper, R.N. Zare, J. Chem. Phys. 48 (1968) 942.
[44] K.J. Reed, A.H. Zimmerman, H.C. Andersen, J.I. Brauman, J. Chem. Phys. 64 (1976) 1368.
[45] R. Gygax, H.L. McPeters, J.I. Brauman, J. Am. Chem. Soc. 101 (1979) 2567.
[46] D. Dill, J. Chem. Phys. 65 (1976) 1130.
[47] N. Chandra, Chem. Phys. 108 (1986) 301.
[48] H. Rudolph, V. McKoy, J. Chem. Phys. 91 (1989) 2235.
[49] H.K. Park, R.N. Zare, J. Chem. Phys. 104 (1996) 4554.
[50] H.K. Park, R.N. Zare, J. Chem. Phys. 104 (1996) 4568.
[51] J.L. Dehmer, D. Dill, Phys. Rev. A 18 (1978) 164.
[52] A.V. Golovin, N.A. Cherepkov, V.V. Kuznetsov, Z. Phys. D 24 (1992) 371.
[53] I. Powis, Chem. Phys. Lett. 189 (1992) 473.
[54] K.L. Reid, I. Powis, J. Chem. Phys. 100 (1994) 1066.
[55] S. Kaesdorf, G. Schönhense, U. Heinzmann, Phys. Rev. Lett. 54 (1985) 885.
[56] E. Shigemasa, J. Adachi, M. Oura, A. Yagishita, Phys. Rev. Lett. 74 (1995) 359.
[57] K. Ueda, K. Ohmori, M. Okunishi, H. Chiba, Y. Shimizu, Y. Sato, T. Hayaishi, E. Shigemasa, A. Yagishita, Phys. Rev. A 52 (1995) R1815.
[58] E. Seidl, H.F. Schaefer III, J. Chem. Phys. 96 (1992) 1176.
[59] K.M. Dunn, G.E. Scuseria, H.F. Schaefer III, J. Chem. Phys. 92 (1990) .
[60] J. Goodman, L.E. Brus, J. Chem. Phys. 67 (1977) 4398.
[61] J. Goodman, L.E. Brus, J. Chem. Phys. 67 (1977) 4408.
[62] M. Ukai, K. Kameta, K. Shinsaka, Y. Hatano, T. Hirayama, S. Nagaoka, K. Kimura, Chem. Phys. Lett. 167 (1990) 334.
[63] F. Carnovale, J.B. Peel, R.G. Rothwell, Org. Mass Spectrom. 26 (1991) 201.
[64] H. Helm, C.W. Walter, J. Chem. Phys. 98 (1993) .
[65] H.M. Bevsek, M. Ahmed, D.S. Peterka, F.C. Sailes, A.G. Suits, Faraday Discuss. Chem. Soc. 108 (1997) 131.